Journal of
Polymer Materials

Tech Science Press

https://doi.org/10.32604/jpm.2026.075379

ARTICLE

Study on the Thermo-Mechanical Properties of Boron Phenolic Resin Composites Enhanced by Silicone Resin Modification and Multiple Ceramic Fillers

Mingyan He[1,2], Jiayu Fu[1,2], Fangyu Guo[1,2], Dawei Jiang[1,2,*], Ting Yang[1,2], Miaojun Xu[1,2,*], Zijian Wu[3] and Bin Li[1,2,*]

[1]College of Chemistry, Chemical Engineering and Resource Utilization, Northeast Forestry University, Harbin, China
[2]Heilongjiang Key Laboratory of Molecular Design and Preparation of Flame Retarded Materials, Northeast Forestry University, Harbin, China
[3]Department of Material Science and Technology, Harbin University of Science and Technology, Harbin, China

*Corresponding Authors: Dawei Jiang. Email: daweijiang@nefu.edu.cn; Miaojun Xu. Email: xumiaojun@126.com; Bin Li. Email: libinzh62@163.com

Received: 30 October 2025; Accepted: 16 January 2026; Published: 03 April 2026

ABSTRACT: Phenolic resins are widely used in thermal protection, yet achieving simultaneous improvement in thermal stability and mechanical strength remains challenging. In this work, a vinyl-modified silicone resin (VMTQ) was synthesized and incorporated into a boron phenolic resin (BPF) matrix. Three composite ceramic fillers, Al_2O_3–SiO_2–ZrO_2 (ASZ), Al_2O_3–SiO_2–TiO_2 (AST), and Al_2O_3–SiO_2–MgO (ASM), were further introduced to construct a multi-oxide synergistic reinforcement system. Thermogravimetric analysis shows that the maximum decomposition rate decreases by 0.2–0.3%·min^{-1}, while the ASM/V3/BPF-3 composite exhibits a 74.53% increase in char yield at 800°C and a 163.3°C increase in initial decomposition temperature, confirming its significantly enhanced thermal stability. SEM/EDS and XRD analyses reveal that ASZ, AST, and ASM promote the formation of stable ceramic phases, with ASM generating the densest MgO–Al_2O_3–SiO_2 composite oxide layer. Mechanical testing demonstrates that ASZ improves vertical impact strength by 23.9%, AST increases parallel impact strength by 14.1%, and ASM enhances bending strength by 34.5% (316.8 MPa). These results clearly indicate that the combination of VMTQ modification with multi-oxide ceramic fillers can effectively elevate both the thermal stability and mechanical performance of BPF-based composites, providing a practical pathway for designing high-performance resins for demanding thermal-environment applications.

KEYWORDS: Ceramic packing; silicone resin; high temperature resistance

1 Introduction

Phenolic resin is an important synthetic polymer material, characterized by high temperature resistance, flame retardancy, low smoke emission, and insulation properties. It is widely used in aerospace [1–3], electronics [4], electrical appliances [5], and automotive industries [6–9], providing fireproofing and thermal insulation for equipment and ensuring operational safety. It is also a key raw material for making friction materials and composites, playing a crucial role in modern industrial development [10]. However, under extreme service environments involving high heat flux, strong oxidation and long-term thermal exposure, conventional phenolic and even boron phenolic systems still suffer from insufficient ablation resistance, low residual strength after high-temperature exposure, and the tendency to form porous and cracked char layers, which seriously limit their application in advanced thermal protection systems. Therefore,

developing phenolic-based composites with simultaneously enhanced thermal stability, ablation resistance and mechanical reliability remains a major challenge in this field [11].

Among various modification strategies, boron [12–14] doping has been widely recognized as effective approaches to improve the ceramization ability and high-temperature oxidation resistance of phenolic resins by forming thermally stable B–O structures during pyrolysis. However, despite the excellent flame retardancy and thermal resistance of boron phenolic resins, their practical application in extreme thermal environments is still limited by insufficient thermal stability and a trade-off between high-temperature performance and mechanical strength. Recent studies have explored various modification strategies, including elemental doping [15], hybrid resin systems [16,17], and the incorporation of ceramic fillers [18–20], to address these limitations. Silicone-based modifiers [17,21,22] are particularly attractive due to their ability to form thermally stable Si–O–Si networks and ceramic phases at elevated temperatures, thereby enhancing char stability and thermal resistance. Li et al. [23] prepared silicon-modified phenolic resin (SN) through the esterification reaction of phenolic resin with methyltrimethoxysilane, and then introduced boric acid into SN as a curing agent to synthesize silicon- and boron-modified phenolic resin (SNBA). At high temperatures, a stable silicon oxide and boron oxide protective layer is formed, effectively hindering the penetration of heat and oxygen, while reducing the decomposition rate and smoke generation, allowing the resin to maintain a high char yield even at 900°C. Niu et al. [24] used 3 ONa-POSS as a silicon source to successfully prepare boron-silicon hybrid phenolic resin. The study results showed that B–O–C, B–O–Si, and Si–O–Si were successfully incorporated into the resin framework during the synthesis process, and the addition of 3 ONa-POSS not only promoted its curing process but also significantly improved its thermal stability. Although chemical modification of BPF with silicon and boron allows the modified resin to maintain a high char yield and structural stability under extremely high-temperature conditions, relying solely on the chemical modification with silicon and boron elements still cannot fully meet the comprehensive performance requirements of modern high-performance materials under extreme conditions [25]. Nevertheless, most reported studies mainly focus on single ceramic fillers or simple physical blending, and systematic investigations on multi-oxide synergistic ceramic fillers combined with silicone-modified boron phenolic resin systems are still very limited [26]. Besides, most reported works focus on single-component modification, which often improves thermal stability at the expense of mechanical performance. The synergistic effects of multi-oxide ceramic fillers on both thermal and mechanical properties of boron phenolic resin systems remain insufficiently understood. These challenges highlight the need for a rational design strategy that integrates silicone modification with multi-oxide ceramic reinforcement to achieve balanced thermo-mechanical performance.

Resin-based composite coatings and multifunctional polymer composites have been increasingly applied in thermal protection, corrosion resistance, electromagnetic shielding, and surface functionalization, where the integration of thermal, mechanical, and protective performance is essential [27–29]. Recent studies show that the structural design of resin matrices, combined with tailored inorganic fillers or surface-modified nanoparticles, can significantly enhance stability and functionality under demanding conditions [30–32]. For example, Moradi et al. [33] demonstrated that silane-modified CeO_2 nanoparticles can effectively improve the interfacial compatibility and functional performance of acrylic composite coatings, highlighting the importance of molecular-level modification strategies in advancing high-performance resin systems. These insights further support the need for developing resin composites that balance lightweight characteristics with reliable thermo-mechanical properties, especially for extreme-environment applications.

Unlike previous studies that rely mainly on single-element modification or individual ceramic fillers, this work introduces a dual-synergistic strategy combining vinyl-silicone modification with multi-oxide ceramic reinforcement, enabling simultaneous improvement of both high-temperature ceramization behavior and mechanical performance. Based on the above research, this paper uses self-made vinyl-modified

silicone resin (VMTQ) as a modifier and systematically investigates the effects of three kinds of compound ceramic fillers, namely Al_2O_3–SiO_2–ZrO_2 (ASZ), Al_2O_3–SiO_2–TiO_2 (AST), and Al_2O_3–SiO_2–MgO (ASM), on the properties of GF-VMTQ/BPF composites. The high-temperature resistance of the composites is evaluated by comparing the static and dynamic ablation performance with and without fillers. The flame retardant mechanism is revealed in combination with the microstructure, and systematic mechanical property tests are conducted on different filler systems to clarify the differential regulation laws of various fillers on the mechanical properties of the materials, providing a basis for filler selection for composite material design with specific mechanical performance requirements The high-temperature resistance mechanisms of composite materials at different temperatures are visually summarized in Fig. 1.

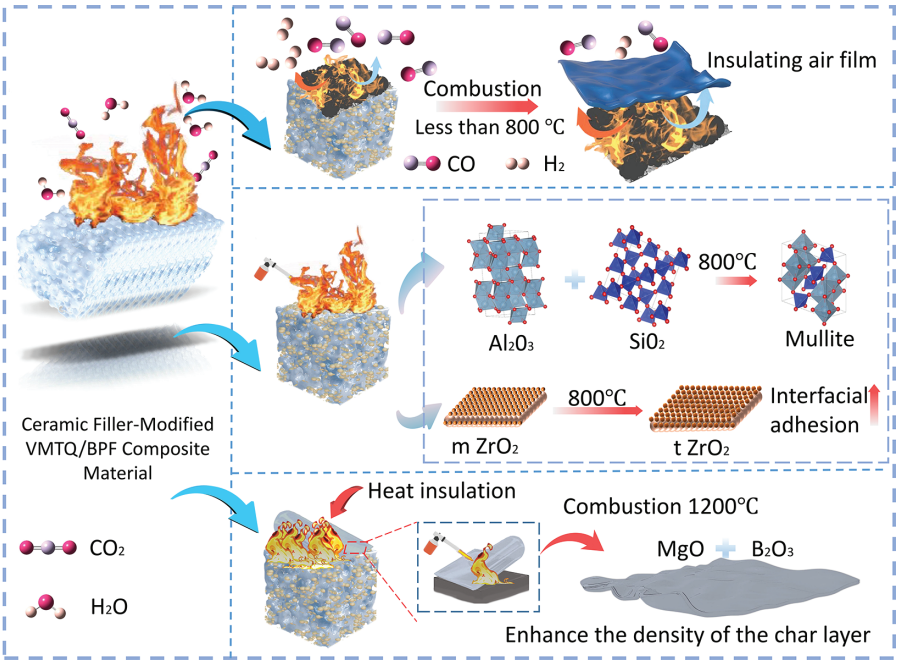

Figure 1: Schematic diagram of the high-temperature resistance mechanism of composite materials at different temperatures.

2 Experimental Section

2.1 Synthesis of VMTQ, VMTQ/BPF and GF-VMTQ/BPF Composite Material

Synthetic scheme of VMTQ silicone resin, fabricated via the hydrolysis-condensation methodology, is displayed in Fig. 2a. The letter M represents hexamethyldisiloxane, a silicon compound with a functionality of 1, T represents vinyltrimethoxysilane, a silicon compound with a functionality of 3, and Q represents tetraethyl orthosilicate, a silicon compound with a functionality of 4. In this experiment, the molar ratio of M, T, and Q structural units in the target polymer used is 3:14:10 [34,35]. Add 1.22 g (7.5 mmol) HMDSO, 5.19 g (35 mmol) VTMO, 3.4 g H_2O, 3 g C_2H_5OH, and 1 mL HAc into a 100 mL round-bottom flask, and under continuous stirring, add 5.21 g (25 mmol) TEOS dropwise at a rate of 2 drops per second. After the dropwise addition is completed, raise the temperature to 70°C and continue stirring the reaction for 6 h. Use rotary evaporation to remove by-products such as methanol, water, and other small molecules generated during the reaction, obtaining a colorless, transparent, viscous VMTQ. Add a certain amount of C_2H_5OH to adjust and obtain a VMTQ ethanol solution with a density of 0.5 g/mL.

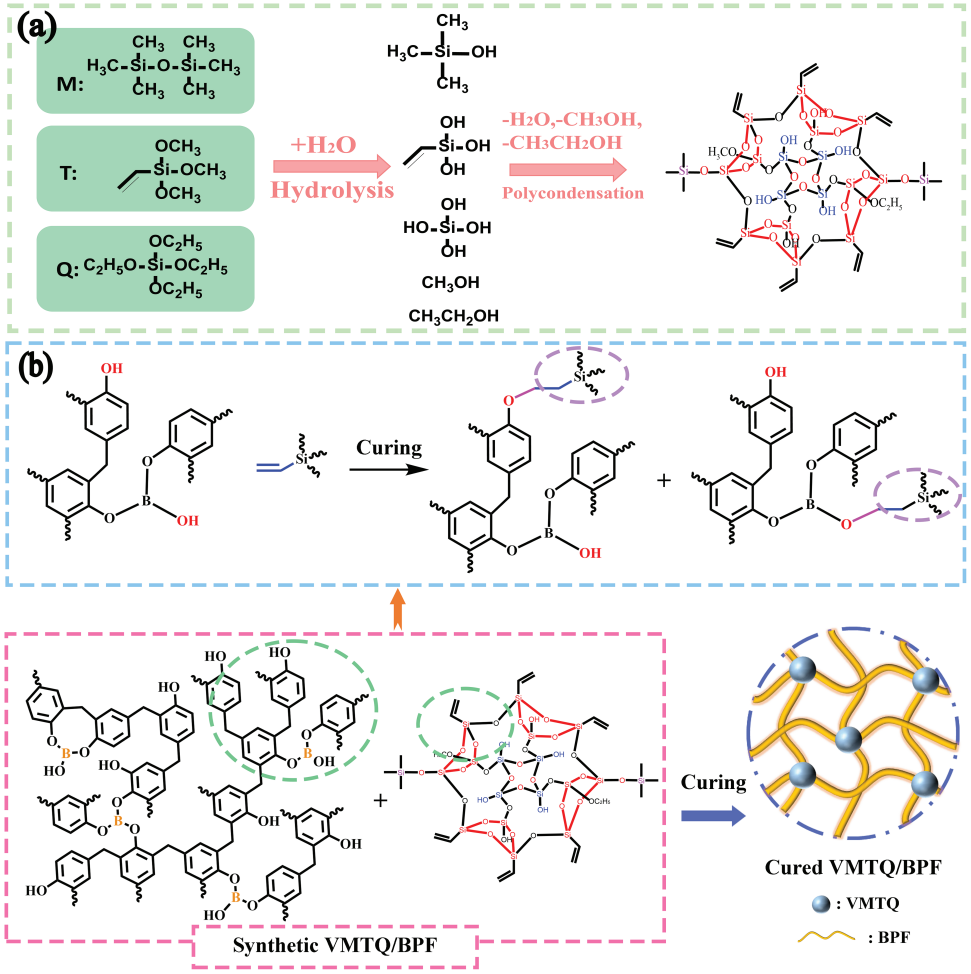

Figure 2: (**a**) Preparation of VMTQ and (**b**) the mechanism of curing crosslinking.

Take a certain amount of BPF powder in a beaker, heat with C_2H_5OH until fully dissolved, then based on BPF, add VMTQ as a modifier in different mass fractions, stir evenly, and cool to room temperature. After stirring evenly, cool to room temperature. Then place it in an electric heating constant temperature blast drying oven, and the curing crosslinking mechanism is shown in Fig. 2b. The formulation is as follows: the mass of BPF is 50.0, 49.5, 48.5, 47.5, 46.5, and 45.5 g, respectively, and the amount of C_2H_5OH is 25.0 g for each. The corresponding masses of VMTQ are 0, 0.5, 1.5, 2.5, 3.5, and 4.5 g, with mass fractions of 0, 1, 3, 5, 7, and 9 wt%, respectively. Weigh BPF powder according to the formulation ratios in Table S1 of the supplementary literature, place it in a beaker, add 25 g of C_2H_5OH and heat until fully dissolved, then add the corresponding amount of VMTQ, stir evenly, and cool to room temperature for later use.

Evenly apply the viscosity-adjusted resin to the surface of the metal plate with a brush, lay a 30 cm × 30 cm GF sheet, continue to apply resin and overlay another layer of fiberglass cloth, and repeat this process until all seven layers of fiberglass cloth are applied. Then bake at 80°C for 30 min, followed by placing it in a flat vulcanizing machine and hot pressing under a pressure of 5 MPa. After hot pressing, allow it to cool naturally to room temperature, demold to obtain the composite material, and cut as needed for future use. To ensure the stability of the adhesive application amount, resins with different VMTQ contents were adjusted for

viscosity with ethanol after cooling, and measured using an NDJ-1 type rotary viscometer. Specific viscosity data are shown in Table S1.

2.2 Preparation of Ceramic Filler-Modified VMTQ/BPF Composites

Based on V3/BPF, composite ceramic fillers were introduced, and composites were prepared with additive amounts of 10%, 20%, and 30%, represented by -1, -2, and -3, respectively, with the ratio of ASZ, AST, and ASM being 5:3:2. The system was mechanically stirred, and after uniform mixing, ethanol was used to adjust the system's viscosity. Then, the system was placed in an ultrasonic cleaner for 1 h of ultrasonic dispersion [19,27]. The ultrasonically dispersed resin system was used to prepare the ceramic-filled composites of each system according to the methods in Section 2.1.

3 Results and Discussion

3.1 VMTQ Structural Characterization Analysis

The VMTQ silicone resin was synthesized via hydrolysis and polycondensation using hexamethyldisiloxane, vinyltrimethoxysilane, and tetraethyl orthosilicate as the starting materials. To determine its chemical structure, Fourier transform infrared (FTIR) spectroscopy and proton nuclear magnetic resonance (^{1}H NMR) spectroscopy were employed for structural characterization. As shown in Fig. 3, the FTIR spectrum, ^{1}H NMR spectrum, and the proposed molecular structure of the VMTQ silicone resin are presented.

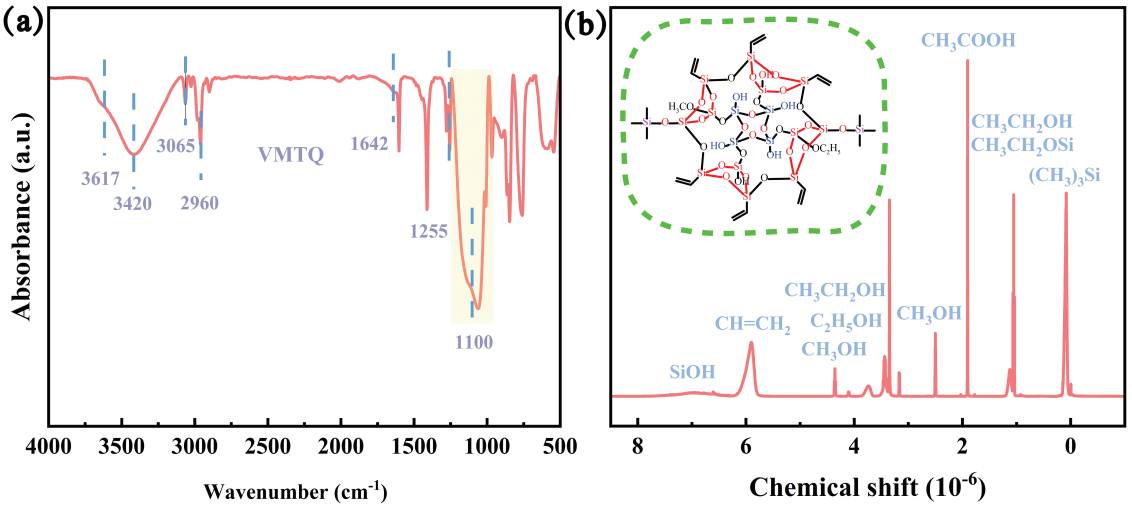

Figure 3: VMTQ siloxane resin (**a**) infrared spectrum, (**b**) ^{1}H NMR spectrum and its structural diagram.

In the FTIR spectrum of VMTQ (Fig. 3a), the absorption peak at 3617 cm^{-1} corresponds to the Si–OH stretching vibration, that at 3420 cm^{-1} is attributed to the O–H bond stretching, the band at 1255 cm^{-1} arises from the symmetric bending vibration of the Si–C bond in Si–CH_3, and the broad band within 1000–1100 cm^{-1} is assigned to the Si–O–Si stretching vibration. These characteristic peaks collectively confirm the occurrence of silane hydrolysis and silanol condensation, suggesting the formation of a cross-linked siloxane network and thereby verifying the successful synthesis of VMTQ.

In the spectrum, in addition to distinct signals from trace acetic acid used for pH adjustment and methanol generated during hydrolysis-condensation, characteristic resonance signals corresponding to the main structural groups of VMTQ were observed: δ = 0.1 ppm for $(CH_3)_3Si$ (trimethylsilyl), δ = 5.9 ppm

for –CH=CH_2 (vinyl), δ = 6.9 ppm for Si–OH (silanol), and δ = 3.8, 3.4, and 1.1 ppm for CH_3CH_2OH, CH_3CH_2O/CH_3O, and CH_3CH_2O groups, respectively, assigned to silylethoxy or silyloxymethyl species. Based on the integrated area ratio of $(CH_3)_3Si$:–CH=CH_2:Si–OH = 3:3:1 and the feed composition, it can be inferred that each VMTQ molecule contains two $(CH_3)_3Si$-groups, six-C_6H_5 groups, and six Si-OH groups, with the corresponding molecular structure illustrated in Fig. 3b. These results collectively confirm that the chemical structure of VMTQ is consistent with its designed molecular architecture

3.2 Study on the High-Temperature Resistance of VMTQ/Ceramic Filler Modified BPF

Static ablation rates of VMTQ/BPF composites at varying temperatures are presented in Fig. 4a. For all samples, the residue rate initially decreases and then increases as the temperature rises. At 400°C, the residue rate of only 7 wt% VMTQ/BPF is slightly higher than that of pure BPF, while at 600°C, only the residue rate of 7 wt% VMTQ/BPF among the tested samples is lower than that of pure BPF. At 800°C, 1000°C, and 1200°C, all VMTQ-containing composites exhibit higher residue rates than pure BPF, indicating that VMTQ effectively enhances the high-temperature performance of the resin. Among all formulations, the 3 wt% VMTQ/BPF sample shows the highest residue rate at each temperature, demonstrating relatively optimal high-temperature properties. However, the overall residue of 3 wt% VMTQ/BPF remains limited, suggesting that VMTQ modification alone cannot substantially improve the high-temperature resistance of BPF resin.

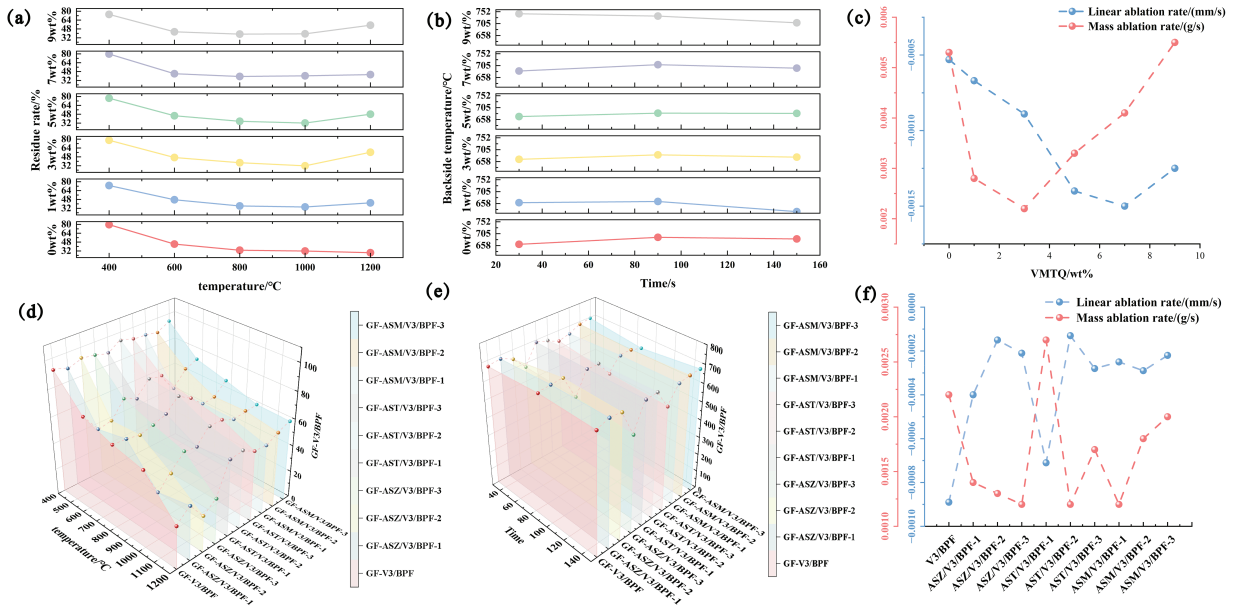

Figure 4: Images of VMTQ/BPF: (**a**) static ablation rate, (**b**) back temperature during ablation, (**c**) linear ablation rate and mass ablation rate, Images of VMTQ/BPF with different modified systems: (**d**) static ablation rate, (**e**) back temperature during ablation, (**f**) linear ablation rate and mass ablation rate.

To further enhance the overall high-temperature protective performance, VMTQ was incorporated into a glass fiber-reinforced BPF composite, and its thermal insulation and ablation resistance were evaluated. As shown in Fig. 4b,c, adding VMTQ enhanced the thermal insulation and ablation resistance of GF-VMTQ/BPF composites. After ablation, all samples exhibited volumetric expansion and formed protruding char layers on their surfaces. This expansion produced negative linear ablation rates, and the degree of expansion increased with the VMTQ content. The 7 wt% sample exhibited the most pronounced expansion, with a linear ablation rate of –0.00150 mm·s^{-1}, representing a 183% increase relative to the GF-BPF matrix

(Fig. 4c). Regarding mass ablation, all VMTQ-modified samples except the 9 wt% one exhibited lower mass ablation rates than the matrix. The 3 wt% sample exhibited the best ablation resistance, with a mass ablation rate of 0.0022 $g{\cdot}s^{-1}$, which is 58.5% lower than that of the matrix, indicating the best overall performance. However, the GF-VMTQ/BPF composite still exhibited a markedly negative linear ablation rate, and the mass ablation rate and overall thermal protection of the 3 wt% sample remained insufficient for higher-temperature applications.

Based on the 3 wt% VMTQ/BPF system, various composite ceramic fillers were introduced. The static ablation rates of each system at different temperatures are shown in Fig. 4d. The residue rates of the modified V3/BPF samples vary notably between 400°C and 1200°C, reflecting the distinct effects of different additives on thermal stability. For the control sample, the residue decreased from 91.9% at 400°C to 32.5% at 1200°C (a variation of 64.6%), indicating pronounced thermal decomposition at high temperatures. In the ASZ/V3/BPF series, all samples exhibited residue rates below 50% at 1200°C. Among them, ASZ/V3/BPF1 showed the highest residue (41.2%) with a 53.7% variation, demonstrating the best performance. The AST/V3/BPF series performed better than the control, particularly between 1000°C and 1200°C, where the decrease in residue rate slowed down. Although AST/V3/BPF1 and AST/V3/BPF2 exhibited similar variation rates, AST/V3/BPF2 consistently retained higher residue values at the same temperatures. At 1200°C, all AST/V3/BPF samples maintained residue rates above 50%, significantly higher than the 32.5% of the control. The ASM/V3/BPF series also exhibited markedly better high-temperature performance than the control. The ASM/V3/BPF series showed excellent thermal stability, with variation rates of 42.1%, 35.9%, and 35.6% for ASM/V3/BPF1, 2, and 3, respectively, all much lower than that of the control. Among these, ASM/V3/BPF3 exhibited the lowest variation rate and the highest residue (60.8%) at 1200°C, indicating superior thermal stability. Based on this system, GF-V3/BPF composites were fabricated and subjected to butane torch ablation tests. The Fig. 4e,f reveal that ceramic fillers substantially modify the ablation response of GF-V3/BPF when subjected to butane torch ablation, suggesting their critical role in thermal protection. After ablation, all samples developed a protruding char layer. However, compared with the system without ceramic fillers, their high-temperature expansion was significantly reduced, attributed to the stable protective layer formed by the fillers that restricted matrix expansion. In terms of ablation resistance, synergistic interactions between the ceramic fillers and the matrix greatly enhanced the high-temperature performance of the composite. Mass loss analysis reveals that, except for the GF-AST/V3/BPF1 sample, all ceramic-filled composites exhibited lower mass ablation rates than the GF-V3/BPF matrix. Among these, GF-ASZ/V3/BPF3, GF-AST/V3/BPF2, and GF-ASM/V3/BPF1 exhibited the best performance, achieving a mass ablation rate of 0.0012 g/s, 45.5% lower than that of the matrix.

Overall, the incorporation of various composite ceramic fillers markedly enhances the high-temperature performance of VMTQ/BPF composites. Different filler systems exhibited distinct trends in residue evolution and high-temperature stability. These findings suggest that composite ceramic fillers effectively suppress excessive matrix expansion under high-temperature conditions, markedly reduce mass loss, and consequently enhance the thermal resistance of VMTQ/BPF composites, meeting the demands of higher-temperature applications.

3.3 High-Temperature Ceramization

A comprehensive analysis of the microstructure and EDS elemental mapping of the three optimal systems, ASZ/V3/BPF1, AST/V3/BPF2, and ASM/V3/BPF3, after treatment at 1200°C reveals their high-temperature structural evolution and characteristic elemental distributions, which clarify the mechanisms underlying their thermal stability and oxidation resistance. As shown in the EDS mappings, carbon, oxygen, aluminum, and silicon are uniformly distributed across all three systems, indicating the formation of stable Al_2O_3 and SiO_2 ceramic phases. In ASZ/V3/BPF1, zirconium appears sparsely and mainly in the form of

ZrO_2. In AST/V3/BPF2, titanium is present as dispersed TiO_2, while boron is homogeneously distributed, suggesting that boron-containing species formed during BPF pyrolysis also participate in constructing the protective layer. In ASM/V3/BPF3, magnesium is uniformly dispersed, confirming the cooperative formation of Al_2O_3-SiO_2-MgO composite oxides capable of effectively suppressing high-temperature decomposition and oxidation.

The SEM images in Fig. 5a,a′ show that ASZ/V3/BPF1 develops an irregular and relatively loose ceramic surface with noticeable roughness, cracks, and pores. These features arise from sintering of Al_2O_3, SiO_2, and ZrO_2 and the volatilization of pyrolysis products. Despite these defects, parts of the surface retain compact, implying the presence of partially continuous oxide layers.

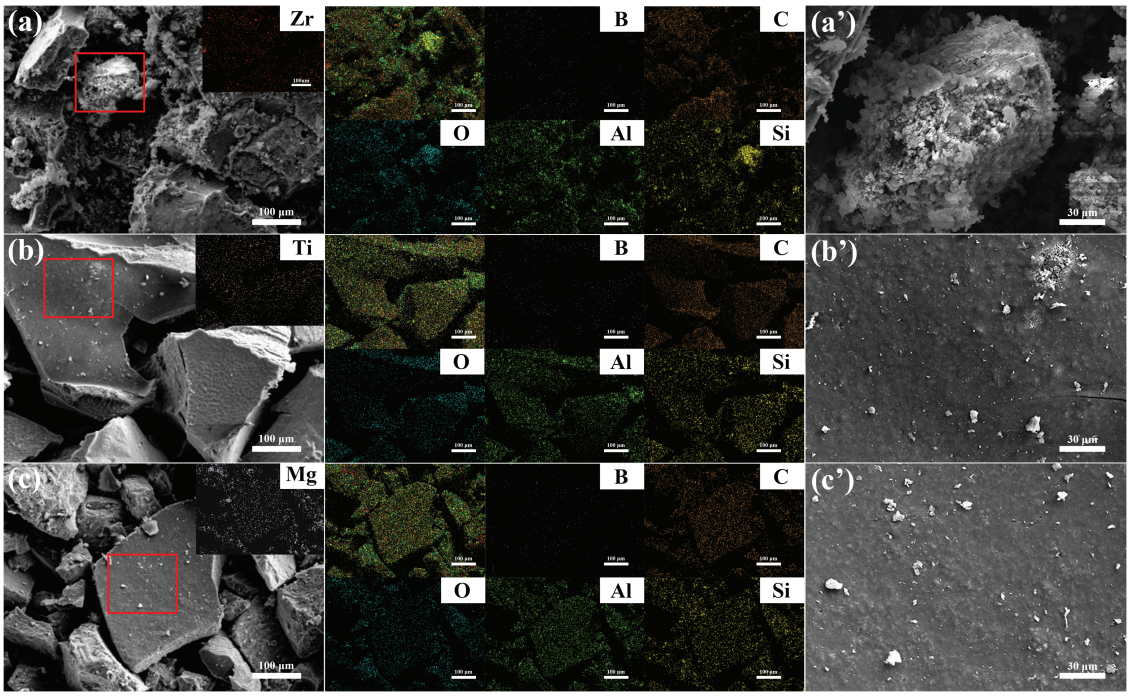

Figure 5: Scanning electron microscopy and EDS elemental mapping of ASZ/V3/BPF1, AST/V3/BPF2, ASM/V3/BPF3 after treatment at 1200°C (**a**–**c**) and enlarged views of selected areas (**a′**–**c′**).

In contrast, ASZ/V3/BPF2 (Fig. 5b,b′) show forms a denser and smoother protective layer, although a few microcracks persist. This layer mainly composed of synergistic oxides of Al_2O_3, SiO_2, and TiO_2, which more effectively inhibit oxidation. ASM/V3/BPF3 (Fig. 5c,c′) exhibits the most compact and uniform ceramic layer, free of visible cracks or pores, demonstrating its superior structural integrity after high-temperature exposure.

The XRD patterns of the three V3/BPF composites with optimal ceramic fillers (ASZ, AST, and ASM) at different temperatures are illustrated in Fig. 6a–c. Over the temperature range of 400°C–800°C, the ASZ, AST, and ASM fillers demonstrated negligible phase or chemical changes while embedded in the resin matrix, suggesting their structural stability under thermal treatment. The XRD patterns mainly exhibit the characteristic diffraction peaks of the fillers, indicating good thermal compatibility between the fillers and the resin in this temperature range. When the temperature increases to 1200°C, distinct differences appear in the XRD patterns of each system. In the ASZ/V3/BPF system, the ZrO_2 crystal structure undergoes a partial phase transformation, with its characteristic diffraction peak shifting from 30.27° to 28.19°, corresponding to a monoclinic-to-tetragonal transition. This shift indicates that elevated temperature induces crystal

reconstruction of ZrO_2. In the AST/V3/BPF system, the diffraction peak of TiO_2 shifts from 25.3° to 27.44°, indicating a transition from the anatase to the rutile phase, a process typically accompanied by lattice densification. In the ASM/V3/BPF system, the intensity of the MgO diffraction peaks at 2θ = 36.9°, 43.02°, and 62.31° significantly increases. This phenomenon is attributed to the healing of crystal defects and lattice reconstruction at elevated temperatures, rather than a simple phase transition. Notably, Al_2O_2 and SiO_2 react with resin pyrolysis products at elevated temperatures to form stable composite oxide phases, consistent with the dense surface layers and uniform elemental distributions observed in the SEM analysis. Although no distinct diffraction peaks of carbon were detected in the XRD patterns, the carbon produced from resin pyrolysis likely exists in an amorphous or microcrystalline state, whose weak signal is masked by the strong diffraction peaks of the fillers.

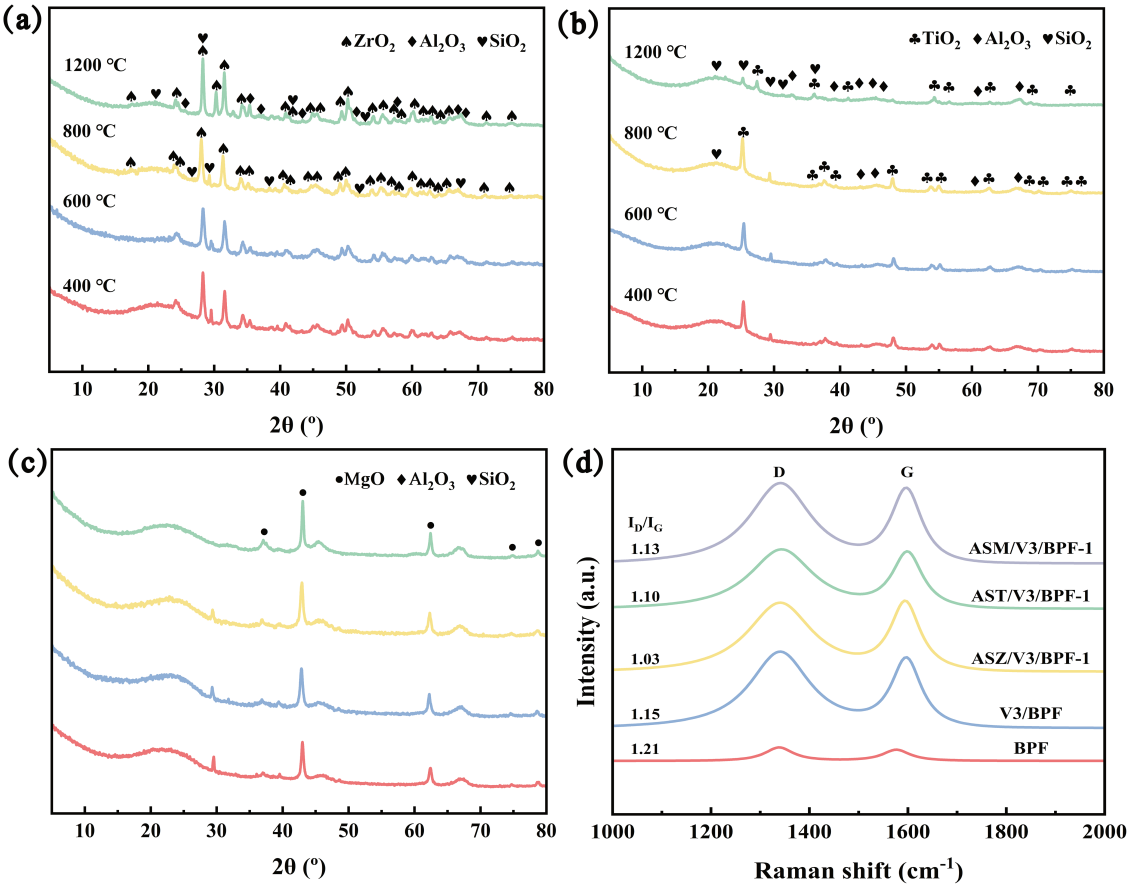

Figure 6: XRD patterns of different systems: (**a**) ASZ, (**b**) AST, (**c**) ASM, (**d**) Raman spectra of BPF, V3/BPF, and V3/BPF1 with added ceramic fillers after high-temperature treatment at 1200°C.

To further explore the promoting effect of ceramic fillers on graphitization during the high-temperature pyrolysis of the VMTQ/BPF system, Raman spectroscopy was performed on the pyrolytic carbon residues of BPF, VMTQ/BPF, and VMTQ/BPF1 composites treated at 1200°C, and their ID/IG ratios were determined (Fig. 6d). The ID/IG ratio serves as a key indicator of structural defects in carbon materials, a lower value corresponds to a higher degree of graphitization and a more ordered structure. Taking the ID/IG value of 1.15 for the V3/BPF system at 1200°C as a reference, the systems containing different ceramic fillers exhibited distinct variations. Among these, ASZ/V3/BPF1 exhibited the lowest ID/IG ratio, markedly lower than that of V3/BPF, indicating the highest degree of graphitization and the fewest structural defects. AST/V3/BPF1

showed an ID/IG value of 1.10, slightly lower than V3/BPF, suggesting moderate graphitization enhancement, whereas ASM/V3/BPF1 presented an ID/IG value of 1.13, close to that of V3/BPF, implying only a slight improvement with relatively high defect density remaining.

3.4 Thermal Stability at High Temperatures

Fig. 7 displays the TGA and DTG curves for the optimal samples of each system. Thermal analysis results (Table S2) indicate that AST/V3/BPF2 and ASM/V3/BPF3 exhibit markedly enhanced thermal stability compared with the other samples, markedly enhances the high-temperature thermal resistance and cracking temperature of the composites. The decomposition temperatures at 5% weight loss ($T_{5\%}$) are 380.2°C and 385.7°C, respectively, much higher than those of V3/BPF (222.4°C) and ASZ/V3/BPF1 (198.6°C). However, considering the early-stage mass loss mainly arises from the evaporation of adsorbed moisture, residual solvents, and the release of small molecules during initial curing, the improvement in $T_{5\%}$ does not reflect a fundamental enhancement in intrinsic decomposition resistance of the resin matrix. At the main decomposition stage ($T_{10\%}$), their decomposition temperatures further increase to 447.9°C and 456.4°C (Fig. 7a), far exceeding those of the comparison samples, demonstrating outstanding thermal stability under elevated temperatures. Meanwhile, the maximum weight-loss rate (V_{max}) decreases to 1.3%·min^{-1} for both AST and ASM systems, compared with 1.6%·min^{-1} for V3/BPF and 1.4%·min^{-1} for ASZ/V3/BPF1 (Fig. 7b), indicating that the degradation process is effectively retarded and becomes more controllable in the presence of ceramic fillers. Moreover, the residual char yields at 800°C for AST/V3/BPF2 and ASM/V3/BPF3 reach 67.8% and 69.2%, respectively, which are markedly higher than those of V3/BPF (58.5 wt%) and ASZ/V3/BPF1 (58.3 wt%). This result confirms that although the fillers do not significantly increase the initial decomposition temperature, they greatly improve the high-temperature structural stability and ultimate thermal endurance of the composites.

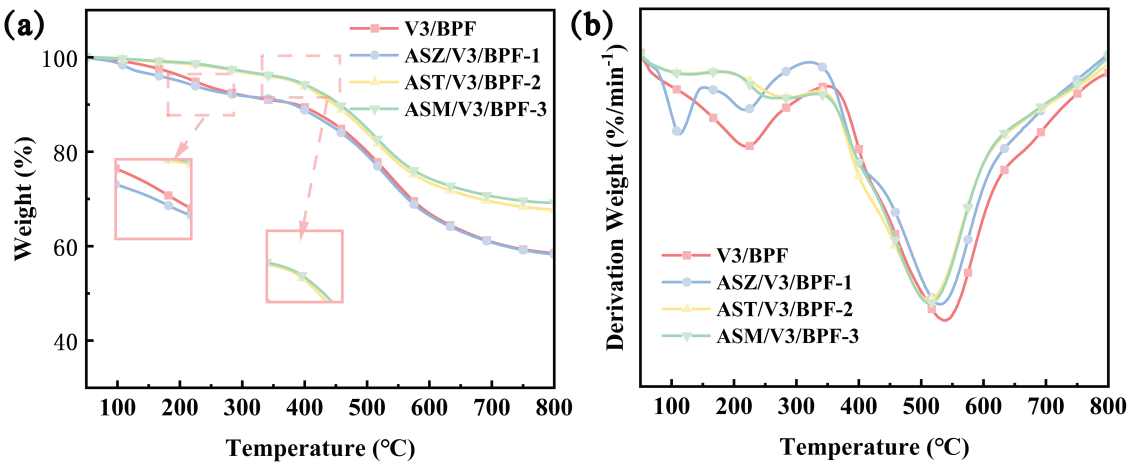

Figure 7: (**a**) TGA and (**b**) DTG curves of the optimal samples of each system.

Combined TGA and XRD analyses reveal that interactions among the components in the ASZ system are relatively weak, dominated by physical mixing rather than chemical synergy, leading to lower char yield and reduced thermal stability compared with the AST and ASM systems. In the AST system, the anatase-to-rutile phase transition of TiO_2 promotes carbon-layer densification and facilitates interfacial bonding with the resin matrix. The ASM system, in contrast, exhibits the strongest ceramic-forming capability. Lattice reconstruction of MgO, together with the formation of Al_2O_3/SiO_2 composite oxides, generates a dense thermal-protective layer. The coexistence of carbon and ceramic phases provides exceptional resistance to

thermal decomposition and ablation at elevated temperatures. Owing to the synergistic ceramic-forming effect of multiple fillers, the ASM/V3/BPF system develops a structurally robust and highly dense composite oxide protective layer at 1200°C, exhibiting optimal thermal stability and ablation resistance.

3.5 Mechanical Properties

The mechanical properties data for GF-ASZ/V3/BPF, GF-AST/V3/BPF, and GF-ASM/V3/BPF composites at different filler contents, presented in Fig. 8, elucidate the distinct impacts of filler type and concentration on the mechanical properties of GF-V3/BPF materials. For the GF-ASZ/V3/BPF system, when the ASZ content is 10%, the vertical and parallel impact strengths reach 163.3 kJ·m^{-2} and 146.8 kJ·m^{-2} (Fig. 8a), respectively. Compared with the control group, the vertical impact strength increases by 23.9%, while the parallel direction remains nearly unchanged, indicating that a moderate ASZ addition effectively enhances vertical impact resistance without compromising in-plane stability. However, excessive filler loading (≥20%) causes a sharp decline in both directions due to internal stress concentration and interface defects, at 30% content, the vertical impact strength drops to 48.1 kJ·m^{-2}. Thus, 10% ASZ is identified as the optimal content for maintaining balanced impact performance. For the GF-AST/V3/BPF system, the AST filler shows a limited effect on vertical impact strength but significantly improves the parallel direction. At 20% content, the parallel impact strength increases to 170.2 kJ·m^{-2}, representing a 14.1% improvement over the control group, while maintaining stable performance in the vertical direction. The optimal formulation, GF-AST/V3/BPF-2, achieves excellent overall impact properties, particularly in the parallel orientation, offering a superior balance of strength and toughness. For the GF-ASM/V3/BPF system, the vertical impact strength remains nearly constant (138.0–139.2 kJ·m^{-2}) across the 10%–30% filler range, with fluctuations below 1%. The parallel direction, however, exhibits a nonlinear trend: enhancement at low content (165.7 kJ·m^{-2} at 10%), decline at 20%, and partial recovery at 30%. The best configuration, GF-ASM/V3/BPF1, achieves stable vertical performance and the highest parallel impact strength, demonstrating effective reinforcement at moderate filler levels.

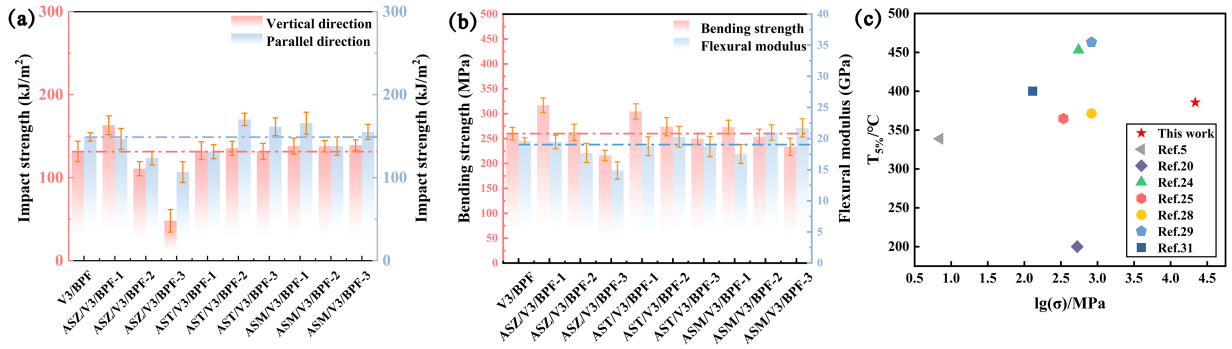

Figure 8: (**a**)Impact strength (**b**) bending strength and flexural modulus under various systems and (**c**) comparison of thermal property and bending strength with recent work.

Bending strength results reveal that the ASZ system most effectively enhances flexural strength, with the ASZ/V3/BPF1 sample reaching 316.8 MPa, substantially exceeding the baseline, though its influence on the flexural modulus is limited (Fig. 8b). Conversely, the AST system exhibits balanced strength and rigidity, with AST/V3/BPF1 and AST/V3/BPF2 maintaining values comparable to or slightly higher than the control. The ASM system excels in stiffness enhancement, as evidenced by the ASM/V3/BPF3 sample achieving a flexural strength of 21.72 GPa, remarkably higher than the baseline, though the flexural pattern improvement remains modest.

In summary, the three filler systems modulate the mechanical behavior of GF-V3/BPF composites through distinct reinforcement mechanisms: ASZ primarily enhances vertical impact strength and flexural strength, AST offers balanced impact and flexural performance, and ASM markedly improves stiffness via modulus enhancement. Therefore, the optimal filler type and content should be selected according to specific performance requirements in practical applications.

In addition, a comparative analysis of performance was conducted by evaluating key parameters (Fig. 8c), including bending strength and $T_{5\%}$. Different systems exhibit distinct trade-offs among individual performance metrics, whereas the material developed in this study demonstrates a more balanced overall performance. From the perspective of thermal stability, some materials reported in the literature exhibit higher $T_{5\%}$ values; however, their bending strength is relatively poor. In contrast, the material in this work maintains a moderately high $T_{5\%}$, reflecting a reasonable balance between thermal stability and mechanical performance. Moreover, in terms of mechanical properties, the bending strength of the material in this work is significantly higher than that reported in the comparative literature, representing one of the most prominent advantages in the radar chart. These results indicate that the present work improves the mechanical load-bearing capacity of the material without sacrificing structural integrity, which is critical for reliability under practical service conditions.

4 Conclusions

In this study, vinyl-modified silicone resin (VMTQ) was synthesized and incorporated into a boron phenolic resin (BPF) system, and three composite ceramic fillers (ASZ, AST, ASM) were introduced to construct a multi-oxide synergistic modification strategy. This approach simultaneously improved the thermal stability, ceramization behavior, and mechanical properties of the composites. TGA/DTG analysis revealed that the incorporation of ASZ, AST, and ASM reduced the maximum decomposition rate (Vmax) by 0.2–0.3%·min^{-1} and enhanced the high-temperature stability of the resin matrix. The ASM/V3/BPF-3 composite exhibited the most significant improvement, with a 74.53% increase in residual weight at 800°C and an elevation of 163.3°C in the initial decomposition temperature. These results demonstrate the strong thermal reinforcement effect of the multi-oxide ceramic fillers. SEM/EDS mapping and XRD analysis further confirmed the formation of stable ceramic phases at elevated temperatures. ASZ and AST promoted the generation of Al_2O_3/SiO_2-based protective structures, while ASM enabled the formation of a dense $MgO–Al_2O_3–SiO_2$ composite oxide layer, leading to superior structural integrity during thermal exposure. Mechanical testing showed that each filler system enhanced different aspects of mechanical performance. ASZ increased vertical impact strength by 23.9%, AST improved parallel impact strength by 14.1%, and ASM yielded the highest bending strength of 316.8 MPa (a 34.5% improvement). These results indicate that the composites can be tailored according to specific engineering requirements.

Overall, this work proposes a novel dual-synergistic modification route, combining silicone network reinforcement with multi-oxide ceramic filler synergy, to achieve concurrent improvement in thermo-oxidative stability and mechanical properties. The findings provide a feasible and effective strategy for designing high-performance resin composites for demanding thermal protection environments.

Acknowledgement: This research was funded by Large-Scale Instrument and Equipment Sharing Service Platform of College of Chemistry, Chemical Engineering and Resource Utilization, NEFU.

Funding Statement: This research was supported by the National Natural Science Foundation of China (Grant No. 52273066) and Undergraduate Training Programs for Innovations by Heilongjiang Province [grant number S202510225421].

Author Contributions: Mingyan He: Conceptualization, methodology, data curation, writing—original draft. Jiayu Fu: Investigation, formal analysis, visualization. Fangyu Guo: Investigation, resources, data analysis. Dawei Jiang: Supervision, project administration, funding acquisition, writing—review & editing. Ting Yang: Methodology, validation, software. Miaojun Xu: Supervision, writing—review & editing. Zijian Wu: Characterization, validation. Bin Li: Conceptualization, supervision, writing—review & editing. All authors reviewed and approved the final version of the manuscript.

Availability of Data and Materials: The data that support the findings of this study are available from the Corresponding Author, Dawei Jiang, upon reasonable request.

Ethics Approval: Not applicable.

Conflicts of Interest: The authors declare no conflicts of interest.

Supplementary Materials: The supplementary material is available online at https://www.techscience.com/doi/10.32604/jpm.2026.075379/s1.

References

1. Poloni E, Bouville F, Schmid AL, Pelissari PIBGB, Pandolfelli VC, Sousa MLC, et al. Carbon ablators with porosity tailored for aerospace thermal protection during atmospheric re-entry. Carbon. 2022;195:80–91. doi:10.1016/j.carbon.2022.03.062.
2. Li J, Pan L, Zhang S, Zhang J, Shi M, Shen Q. Ceramicization mechanism and thermal insulation/ablative properties of hollow microspheres/boron phenolic composites. Polym Degrad Stab. 2023;212:110344. doi:10.1016/j.polymdegradstab.2023.110344.
3. Liu Y, Jiang D, Hessien MM, Mahmoud MHH, Xu M, El-Bahy ZM. Enhanced thermal and mechanical properties of boron-modified phenolic resin composites with multifiller system for aerospace applications. Adv Compos Hybrid Mater. 2024;7(5):180. doi:10.1007/s42114-024-00961-z.
4. Sharma A, Kumar R, Gupta A, Agrawal PR, Dwivedi N, Mondal DP, et al. Enhanced electromagnetic interference shielding properties of phenolic resin derived lightweight carbon foam decorated with electrospun zinc oxide nanofibers. Mater Today Commun. 2022;30:103055. doi:10.1016/j.mtcomm.2021.103055.
5. Dey SC, Worfolk B, Lower L, Sagues WJ, Nimlos MR, Kelley SS, et al. Phenolic resin derived hard carbon anode for sodium-ion batteries: a review. ACS Energy Lett. 2024;9(6):2590–614. doi:10.1021/acsenergylett.4c00688.
6. Song W, Park J, Seo H, Choi J, Lee JJ, Sohn SS, et al. Reduction of brake emission by optimizing the curing condition for brake pads using an artificial neural network. Wear. 2023;516:204606. doi:10.1016/j.wear.2022.204606.
7. Matějka V, Lu Y, Matějková P, Smetana B, Kukutschová J, Vaculík M, et al. Possible stibnite transformation at the friction surface of the semi-metallic friction composites designed for car brake linings. Appl Surf Sci. 2011;258(5):1862–8. doi:10.1016/j.apsusc.2011.10.063.
8. Fernandes GP, Zanotto PS, Sinatora A. Contribution on understanding the friction film development in the performance of a dry automotive clutch system. Wear. 2015;342:364–76. doi:10.1016/j.wear.2015.09.007.
9. Tadini P, Grange N, Chetehouna K, Gascoin N, Senave S, Reynaud I. Thermal degradation analysis of innovative PEKK-based carbon composites for high-temperature aeronautical components. Aerosp Sci Technol. 2017;65(3):106–16. doi:10.1016/j.ast.2017.02.011.
10. Yin R, Cheng H, Hong C, Zhang X. Synthesis and characterization of novel phenolic resin/silicone hybrid aerogel composites with enhanced thermal, mechanical and ablative properties. Compos Part A Appl Sci Manuf. 2017;101:500–10. doi:10.1016/j.compositesa.2017.07.012.
11. Zhang Y, Liu Y, Jiang D, Shalash M, El-Bahy SM, Wu Z, et al. A comprehensive review on modified phenolic resin composites for enhanced performance across various applications. Polym Compos. 2025;46(10):8731–69. doi:10.1002/pc.29537.
12. Xing X, Zhang P, Zhao Y, Ma F, Zhang X, Xue F, et al. Pyrolysis mechanism of phenylboronic acid modified phenolic resin. Polym Degrad Stab. 2021;191:109672. doi:10.1016/j.polymdegradstab.2021.109672.

13. Wang S, Jing X, Wang Y, Si J. High char yield of aryl boron-containing phenolic resins: the effect of phenylboronic acid on the thermal stability and carbonization of phenolic resins. Polym Degrad Stab. 2014;99:1–11. doi:10.1016/j.polymdegradstab.2013.12.011.
14. Abdalla MO, Ludwick A, Mitchell T. Boron-modified phenolic resins for high performance applications. Polymer. 2003;44(24):7353–9. doi:10.1016/j.polymer.2003.09.019.
15. Du Y, Xia Y, Luo Z, Yuan W, Xu K, Wang Q, et al. An addition-curable hybrid phenolic resin containing silicon and boron with improved thermal stability. Polym Degrad Stab. 2021;189:109599. doi:10.1016/j.polymdegradstab.2021.109599.
16. Chen L, Nie X, Zhang P, Wang Q, Hu C, Lei Z, et al. Boron-silicon hybrid phenolic composites modified by Ti_3AlC_2 MAX phase and microcapsules for wide-temperature, long-duration thermal protection. Compos Part B Eng. 2026;310:113183. doi:10.1016/j.compositesb.2025.113183.
17. Huang H, Lv Y, Jin X, Wang H, Wu C, Pan Y, et al. Bifunctional silicone triggered long-range crosslinking phenolic aerogels with flexibility and thermal insulation for thermal regulation. Chem Eng J. 2023;470:144413. doi:10.1016/j.cej.2023.144413.
18. Li Z, Li Y, Shen Y, Yu T, Wang J. Synergic effects of dimethyl methylphosphonate (DMMP) and nano-sized montmorillonite (MMT) on the flammability and mechanical properties of flax fiber reinforced phenolic composites under hydrothermal aging. Compos Sci Technol. 2022;230:109487. doi:10.1016/j.compscitech.2022.109487.
19. Mirzapour A, Asadollahi MH, Baghshaei S, Akbari M. Effect of nanosilica on the microstructure, thermal properties and bending strength of nanosilica modified carbon fiber/phenolic nanocomposite. Compos Part A Appl Sci Manuf. 2014;63:159–67. doi:10.1016/j.compositesa.2014.04.009.
20. Gao L, Jiang D, Wu Z, Jiang B, Xu Q, Xu M. Emerging fabrication of ceramic nanofiber aerogel with the application in high-temperature thermal insulation, environment, and electromagnetic wave absorption. Colloid Polym Sci. 2024;302(8):1169–200. doi:10.1007/s00396-024-05255-w.
21. Zhong H, Hu H, Ni B, Guo Y, Luo Z, Zhao T, et al. Silica sol nanoparticles hybridized allyl phenolic resins for improving mechanical and thermal performance. Polymer. 2022;254:125052. doi:10.1016/j.polymer.2022.125052.
22. Gao D, Nie J, Cai M, Ju M, Liang Y, Zhang X. Silica sol modified phenolic resin and its effect on mechanical properties of Al_2O_3-SiC-C bricks. J Eur Ceram Soc. 2023;43(15):7189–95. doi:10.1016/j.jeurceramsoc.2023.07.022.
23. Li S, Chen F, Zhang B, Luo Z, Li H, Zhao T. Structure and improved thermal stability of phenolic resin containing silicon and boron elements. Polym Degrad Stab. 2016;133:321–9. doi:10.1016/j.polymdegradstab.2016.07.020.
24. Niu Z, Xin Y, Wang L, Shen S, Ma X, Chen B, et al. Two birds with one stone: construction of bifunctional-POSS hybridized boron-silicon ceramicized phenolic composites and its ablation behavior. J Mater Sci Technol. 2023;141:199–208. doi:10.1016/j.jmst.2022.10.004.
25. Li J, Bian R, Liu P, Wang Z, Lyu Y, Li X, et al. A tough, strong, and fast-curing phenolic resin enabled by quercetin-functionalized hyperbranched polymer. Ind Crops Prod. 2024;222:119721. doi:10.1016/j.indcrop.2024.119721.
26. Xin Y, Niu Z, Shen S, Ma X, Chen F, Wang L, et al. A novel B-Si–Zr hybridized ceramizable phenolic resin and the thermal insulation properties of its fiber-reinforced composites. Ceram Int. 2023;49(3):4919–28. doi:10.1016/j.ceramint.2022.10.006.
27. Naderi A, Mazinani S, Javad Ahmadi S, Sohrabian M, Arasteh R. Modified thermo-physical properties of phenolic resin/carbon fiber composite with nano zirconium dioxide. J Therm Anal Calorim. 2014;117(1):393–401. doi:10.1007/s10973-014-3742-2.
28. Pan Y, Jin X, Wang H, Huang H, Wu C, Yan X, et al. Nano-TiO_2 coated needle carbon fiber reinforced phenolic aerogel composite with low density, excellent heat-insulating and infrared radiation shielding performance. J Mater Sci Technol. 2023;152:181–9. doi:10.1016/j.jmst.2022.12.035.
29. Wang F, Huang Z, Guo Z. Bionic boron/silicon-modified phenolic resin system with multifunctional groups: synthesis, thermal properties and ablation mechanism. Biosurf Biotribol. 2018;4(3):85–93. doi:10.1049/bsbt.2018.0013.
30. Fan LZ, He H, Nan CW. Tailoring inorganic-polymer composites for the mass production of solid-state batteries. Nat Rev Mater. 2021;6(11):1003–19. doi:10.1038/s41578-021-00320-0.

31. Li F, Zhang Z, Qin F, Liang J, Dang W, Zhang X, et al. Zr modified phenolic resin/silica fiber composites with enhanced mechanical properties and ablation resistance: comparison of three different modification routes. Polym Degrad Stab. 2025;242:111700. doi:10.1016/j.polymdegradstab.2025.111700.
32. Kumar A, Ranjan C, Kumar K, Reddy MH, Babu BS, Katiyar JK. State-of-the-art on advancements in carbon-phenolic and carbon-elastomeric ablatives. Polymers. 2024;16(11):1461. doi:10.3390/polym16111461.
33. Moradi N, Jamshidi M, Ghamarpoor R, Moghbeli MR. Surface functionalization/silane modification of CeO_2 nanoparticles and their influences on photocatalytic activity of acrylic films for methylene blue removal. Prog Org Coat. 2023;183:107787. doi:10.1016/j.porgcoat.2023.107787.
34. Han X, Zheng W, Hao J, Wang H, Zhu L, Zhou C. Enhancing the damping and mechanical properties of phenyl silicone rubber by introducing phenyl MQ silicone resins as molecular fillers. Compos Commun. 2024;51:102082. doi:10.1016/j.coco.2024.102082.
35. Zhu J, Zheng J, Hu Y, Wei J, Ma Y, Gou H, et al. Facile fabricated transparent anti-smudge coating with high hardness and excellent flexibility from MTQ and branched silicone resins. Prog Org Coat. 2023;185:107907. doi:10.1016/j.porgcoat.2023.107907.